PCCP

Rotational spectroscopy of the argon dimer by time-resolved Coulomb explosion imaging of rotational wave packets

Journal:	*Physical Chemistry Chemical Physics*
Manuscript ID	CP-ART-03-2022-001113.R1
Article Type:	Paper
Date Submitted by the Author:	14-Apr-2022
Complete List of Authors:	Mizuse, Kenta; Tokyo Institute of Technology, Deparrtmen of Chemistry; Kitasato University Sato, Urara; Kitasato University Tobata, Yuya; Tokyo Institute of Technology, Departmen of Chemistry Ohshima, Yasuhiro; Tokyo Institute of Technology, Departmen of Chemistry

ARTICLE

Rotational spectroscopy of the argon dimer by time-resolved Coulomb explosion imaging of rotational wave packets

Receive$D_0$0th January 20xx,
Accepte$D_0$0th January 20xx

DOI: 10.1039/x0xx00000x

Kenta Mizuse,*[a,b] Urara Sato,[b] Yuya Tobata,[a] and Yasuhiro Ohshima*[a]

We report time-domain rotational spectroscopy of the argon dimer, Ar_2, by implementing time-resolved Coulomb explosion imaging of rotational wave packets. The rotational wave packets are created in Ar_2 with a linearly polarized, nonresonant, ultrashort laser pulse, and their spatiotemporal evolution is fully characterized by measuring angular distribution of the fragmented Ar^+ promptly ejected from Ar_2^{2+} generated by the more intense probe pulse. The pump-probe measurements have been carried out up to a delay time of 16 ns. The alignment parameters, derived from the observed images, exhibit periodic oscillation lasting for more than 15 ns. Pure rotational spectrum of Ar_2 is obtained by Fourier transformation of the time traces of the alignment parameters. The frequency resolution in the spectrum is about 90 MHz, the highest ever achieved for Ar_2. The rotational constant and the centrifugal distortion constant are determined with much improved precision than the previous experimental results: B_0 = 1.72713 ± 0.00009 GHz and D_0 = 0.0310 ± 0.0005 MHz. The present B_0 value does not match within the quoted experimental uncertainty with that from the VUV spectroscopy, so far accepted as an experimental reference to assess theories. The present improved constants would stand as new references to calibrate state-of-the-art theoretical investigations and an indispensable experimental source for the construction of an accurate empirical intermolecular potential.

1 Introduction

Among vast number of studies on non-covalent interaction, pairwise interaction between rare-gas atoms has been deserving particular importance for several reasons. First, the potential energy surface pertinent to the interaction can be described with a single coordinate, i.e., the interatomic distance, owing to the spherical nature of the constituents. Second, the interaction exclusively originates from the exchange repulsion and the attractive dispersion, both of which are ubiquitous between any atoms and molecules.[1, 2]

Among many combinations of homo- and hetero-rare gas atoms, the Ar-Ar system has been extensively studied both by theory and experiments.[3] Accumulated experimental data on bulk properties of gaseous argon (*e.g.* viscosity, second virial coefficients, and thermal conductivity) and scattering cross sections of the Ar-Ar elastic collision have been implemented to construct accurate semiempirical potentials for the Ar pairwise interaction.[4-12] With regard to quantum chemical calculations, recent progresses in computational methodology and resources have provided capability for deriving highly accurate *ab initio* potentials, which satisfactorily reproduce the experimental data reported so far.[13-18] In some cases, precisions of the predicted properties (*e.g.* virial coefficients) with the *ab initio* potentials are below the statistical errors of the experiments.[16-18] Precise evaluation and refinement of *ab initio* or semiempirical potentials have demanded additional experimental inputs with higher accuracies.

As available experimental data, results from spectroscopic measurements on the weakly bound argon dimer, Ar_2, are particularly valuable for detail characterization of the well region of the pair potential. Experimentally derived vibrotational energy-level intervals are directly compared with eigen-energies of bound levels calculated on the potential. In addition, when frequency resolution of the measurements is high enough to observe rotational fine structures, the rotational constants can be determined to give precise information on vibrationally averaged inter-atomic distance of the system. Since the argon dimer is a homonuclear diatomic molecule, microwave and infrared spectroscopy cannot be applied to it, as opposed to mixed rare gas dimers, of which pure rotational spectra have been observed.[19-21] The spectroscopic study of the Ar_2 was initiated in 1970 by Tanaka and Yoshino, who measured its electronic absorption spectrum from the $^1\Sigma_g^+$ electronic ground state in the vacuum ultraviolet (VUV) region.[22] Later, spectral resolution and sensitivity were improved to obtain its rotationally resolved emission spectra.[23, 24] In 1988, Herman *et al.* adopted laser-induced-fluorescence (LIF) detection with a laser-based tunable VUV source to achieve the frequency resolution of 0.2–0.3 cm^{-1}.[25] From the observed rotationally resolved VUV vibronic spectrum of the adiabatically cooled Ar_2, the ground-state rotational constant B_0 and the centrifugal-distortion constant D_0 was determined in the $^1\Sigma_g^+$ manifold, as

[a] Department of Chemistry, School of Science, Tokyo Institute of Technology, 2-12-1-W4-9 Ookayama, Meguro, Tokyo 152-8550, Japan. E-mail: ohshima@chem.titech.ac.jp (Y.O.)
[b] Department of Chemistry, School of Science, Kitasato University, 1-15-1 Kitazato, Minami, Sagamihara, Kanagawa 252-0373, Japan. E-mail: mizuse@kitasato-u.ac.jp (K.M.)

shown in Table 1. In the theoretical studies, the B_0 constant has been calculated by computing eigen-energies for several values of rotational angular momentum J on a semiempirical or *ab initio* pair potential.[9, 13-18, 26] Table 1 also collects some of theoretically predicted values of B_0, accompanied with the experimental results. The theoretical values are within the range of 0.0570–0.0578 cm^{-1}, and those on the *ab initio* potentials from highly correlated levels with substantially large basis sets are converged to ~0.05760 cm^{-1}.[16, 18, 26] Its difference from the VUV-LIF results[25] is 1.6×10^{-4} cm^{-1}, substantially exceeding the experimental uncertainty of 0.6×10^{-4} cm^{-1}. Boyes reanalysed the VUV-LIF data by including low-J transitions, which had been discounted in the original analysis, as well as by taking the higher centrifugal distortion term into account.[10] The resultant values of B_0 is smaller by 2.2×10^{-4} cm^{-1} from the original one, as listed in Table 1, yielding to much improved agreement with the recent theoretical results. Still the original value of B_0 has been quoted as a reference for evaluation and construction of pair potentials.[9, 12]

Table 1. Reported ground-state rotational constants and centrifugal-distortion constants of $^{40}Ar_2$.

B_0/cm^{-1}	$10^6 \times D_0$ /cm^{-1}	Method	Year (reference)
0.05778	1.13	VUV [a]	1976 (ref 23)
0.05776(6)	1.22(4)	VUV [a]	1988 (ref 25)
0.05777		HFDID1 [b]	1993 (ref 9)
0.05755(11)	1.05(5)	Reanalysis of VUV	1994 (ref 10)
0.05708		CCSD(T)/a5Z+ [c]	1999 (ref 13)
0.05745		CCSD(T)/a6Z+ [c]	2003 (ref 14)
0.05743		CCSD(T)/a6Z+/CBS [c]	2005 (ref 15)
0.05760		CCSDT(Q)/a6Z+ [c]	2009 (ref 16)
-		CCSDTQ/a6(7)Z+ [c]	2010 (ref 18)
0.05756(4)		RWP [d]	2011 (ref 29)
0.0576(1)		RWP [d]	2014 (ref 30)
0.057432	1.02	Bound-state calc. on ref. 15 potential [e]	2019 (ref 26)
0.057589	1.03	Bound-state calc. on ref. 18 potential [e]	2019 (ref 26)
0.057611(4)	1.03(2)	RWP [d]	2022 (This study)

[a] Vacuum ultraviolet absorption/fluorescence excitation.

[b] Results from semiempirical pair potential.

[c] Results from quantum chemical calculation. Level of theory adopted therein is indicated for representative purpose. Some of the values listed here were the results after corrections, modifications, and combinations of several methods. Details are given in the references.

[d] Rotational wave-packet imaging.

[e] B_0 and D_0 were obtained by fitting the reported energy levels up to $J = 14$.

Another approach to record rotational spectrum of homo-diatomic species is the measurements of Raman scattering in low-frequency region. Actually, a pioneering study by Godfried and Silvera at around the same time of the VUV laser experiments reported successful observation of spontaneous rotational Raman signals.[27, 28] The spectral resolution (~0.1 cm^{-1}) was barely enough to separately observe rotational lines exhibiting Stokes shifts of a few cm^{-1}, but no spectroscopic constant was reported. More than two decades later, a time-domain variant of rotational Raman spectroscopy was implemented to derive the B_0 constant of Ar_2.[29, 30] A nonresonant ultrashort pulse was irradiated on to the dimer to induce coherent rotational excitation via impulsive stimulated Raman scattering (ISRS) and the resultant time propagation of the molecular orientation of Ar_2 in the vibronic ground state was captured via Coulomb explosion imaging (CEI) triggered by time-delayed another ultrashort pulse. Such a combination of ISRS pump and time-delayed CEI probe was originally developed to observe transient molecular-axis alignment in space in covalently-bound stable molecules, *e.g.* I_2 and N_2,[31-33] and has been extensively applied to track the spatiotemporal evolution of the rotational wave packets in various molecular systems.[34-36]

Wu *et al.* demonstrated the first rotational wave-packet imaging of Ar_2 by using a cold target recoil ion momentum spectrometer (COLTRIMS).[29] They analysed angular distribution of the recoiled Ar^+ fragments upon Coulomb explosion, and evaluated time-dependent alignment parameter. Observed time trace of the parameter shows a clear revival structure with a period of 289.74 ps. From this revival period, they determined the B_0 constant with the precision comparative to the VUV result,[25] as listed in Table 1. The value agrees with those from the high-level *ab initio* calculation, while its deviation from the original VUV-LIF result exceeds the experimental uncertainty. Three years later, Veltheim *et al.* conducted rotational wave-packet imaging of Ar_2 again by using a similar setup to Wu *et al.* and determined the B_0 and D_0 constants from the rotational energy intervals evaluated by the Fourier transformation of the time-dependent alignment parameters, as also listed in Table 1.[30] The reported value of B_0 agrees with the results of the previous experimental and theoretical studies within the quoted uncertainty, though its precision is inferior to the previous experiments.

Frequency resolution in time-domain spectroscopy is in relation of Fourier transformation to the time bandwidth of the measurements. Maximum pump-probe delay time has to be extended to achieve higher resolution. Wu *et al.* carried out the measurements with delay time up to 1 ns, leading to ~GHz (~0.03 cm^{-1}) frequency resolution.[29] To improve the precision of the rotational constants by an order of magnitude, pump-probe delay of more than 10 ns should be realized while keeping sub-picosecond time resolution. Such an extensive pump-probe imaging experiment will be highly demanding for CORTRIMS measurements, of which data acquisition rate is typically one or less ions per single laser shot. Recently, our research group has developed an ion-imaging apparatus with high spatial resolution, providing a way of taking detailed rotational wave-packet movies.[37-39] Our apparatus utilizes a two-dimensional (2D) ion detector, with which a few tens of ions can be detected per laser shot. Such high multi-hit capability is crucial for achieving high frequency resolution in time-resolved imaging. In the present study, we combine our ion-imaging system with a folded optical-delay setup providing the pump-probe delay up

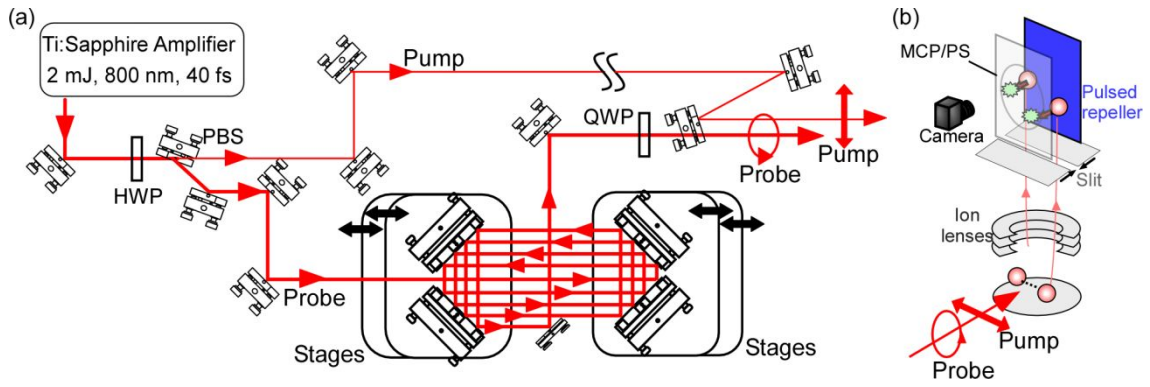

Fig. 1 (a) Schematics of the present pump-probe setup with a long optical delay. HWP: a half wave plate; QWP: a quarter wave plate; PBS: a polarizing beam splitter. (b) Schematic of the 2D space-slice ion imaging setup. MCP: a stack of two microchannel plates; PS: a phosphor screen.

to >10 ns and utilize it to time-domain rotational spectroscopy of Ar_2 with frequency resolution of <100 MHz. The rotational and centrifugal-distortion constants of $^{40}Ar_2$ have been determined with much improved precision, and they are compared with the experimental and theoretical results so far reported.

2 Experimental

Rotational wave-packet dynamics of Ar_2 was visualized by time-resolved Coulomb explosion imaging using a folded pump-probe optical setup and a space-slice ion imaging apparatus. Figure 1 shows schematics of the setup. Experimental scheme and details of the imaging setup were reported elsewhere.[37] Here brief descriptions on the imaging setup are given. Essential details of optical setup are reported.

Figure 1a shows a schematic of the folded pump-probe optical setup. Fundamental output of a Ti:Sapphire laser amplifier (~40 fs, 2 mJ, 800 nm; Quantronix, Odin-II HE) was split into two part: a pump for a creation of rotational wave packets and a probe for Coulomb explosion. The pump pulse passed through a glass block stretcher, and temporal duration of the pulse was prolonged to ~1.3 ps (FWHM). Such a pulse elongation is beneficial to suppress unwanted strong-field/ multiphoton ionization while increasing the pump pulse energy for effective rotational excitation. Since the temporal width of ~1.3 ps is much shorter than the rotational period of Ar_2 (~ 300 ps), the pump pulse exerts nonadiabatic interaction (impulsive Raman excitation) on Ar_2, leading to the creation of rotational wave packets. A half-wave plate and a polarizer were also installed in the pump path to tune the pulse energy and improve the degree of polarization. The probe pulse was time-delayed via a folded optical delay line, and converted to a circularly polarized pulse by a pair of half and quarter wave plates. The pump and probe pulses thus generated were combined and colinearly introduced into the imaging vacuum chamber, and then they are focused onto a molecular beam by a spherical mirror (f = 75 mm). Temporal duration of the probe pulse at the probing region was estimated to be ~55 fs, following a FROG measurement (Swamp Optics, GRENOUILLE, 8-20-USB). Peak intensities of the pump and probe pulses at the focal point were estimated to be 15 TW/cm^2 and 1.2 PW/cm^2, respectively.

The present folded delay line consists of four feedback-looped 20-cm linear stages (SigmaKoki, HST(GS)-200X/ KST(GS)-200X) and four 4-inch diameter mirrors. Two linear stages are stacked, and the two stacks are installed in an opposed manner. Two of 4-inch mirrors form a retro-reflector, and each reflector lies on a stack of stages. Owing to large effective area of the mirrors, a ~9 mm-diameter probe beam can be reflected four times at one mirror. In total, scan range of the present delay line reaches to 0.2 m (stage length) × 4 (number of stages) × 4 (number of loops) × 2 (back-and-forth) = 6.4 m, leading to a temporal delay of up to 20 ns, corresponding to the possible highest frequency resolution of 50 MHz. We found that due to imperfect flatness of the stages and ineligible escape of the pumped species, traveling in the flow of the molecular beam before they are probed, it is difficult to achieve a uniform periodic time-dependent signals during the ~20 ns experiments. Degradation of a time trace results in lower frequency resolution in Fourier-transformed spectrum. In the present setup, typical resolution was ~90 MHz. This point is also discussed in Results and Discussion section.

The absolute pump-probe delay time is given by the difference in the pump and probe optical path lengths divided by the speed of light in the laboratory. Our stages utilize a glass scale-based, sub-micron precision feedback loop through a 0.2 m scan, leading to at least 6 orders of magnitude of accuracy for the path length. To evaluate speed of light in ambient condition, the refractive index of air n_{air} during the experiments was evaluated by monitoring room temperature, relative humidity, and atmospheric pressure. Ciddor's equation was used to calculate instantaneous refractive indexes.[40] The value of n_{air} in a typical day was kept at 1.000261±0.000003, leading to 7-digit precision. We note that when weather conditions changed significantly during the measurements, n_{air} changed by up to 5 × 10^{-6}, limiting experimental accuracy and precision.

For sample preparation, a gaseous mixture of Ar in He (5–10 % Ar; total pressure 3 MPa) was adiabatically expanded into a vacuum chamber through an Even-Lavie pulsed valve,[41] operated at 250 Hz. After passing through two skimmers, the molecular beam was interacted with pump and probe pulses in the middle of ion lens optics (Fig. 1b). Upon circularly polarized probe irradiation, Ar_2 in a molecular beam was multiply ionized and then exploded to Ar^+, without orientational preference for

Ar_2 in the polarization plane of the circularly polarized probe pulse. Three-dimensionally expanding fragmented Ar^+ cloud was accelerated, and a central part of the cloud was sliced out by a 2-mm-width slit installed in the drift region of the imaging apparatus. The ion "sheet" parallel to the probe polarization was then pushed onto the off-axis 2D imaging detector (a stack of microchannel plates backed by a phosphor screen and a digital camera), of which plane is also parallel to the polarization plane. The angular distribution of Ar^+ in the observation plane is a direct measure of dimer-axis distribution at the probed timing. The observation plane includes the symmetry axis of the dynamics (direction of the pump pulse polarization). The observed images, therefore, contains full 3D information in angular coordinate.

3 Results and Discussion

Figure 2a shows an ion image of Ar^+ recorded with the probe pulse alone. In the central part of the image, an enormous number of ions from Ar atoms in a beam could appear. To avoid potential damage to the detector and loading of unnecessary signal data, we installed a mask, a keyhole-shaped aluminum plate, in front of the detector, as shown in Fig. 2a. In the observed image, ring-shaped ion signals were observed. Such a distribution indicates that the Ar^+ ions are ejected with a finite kinetic energy from randomly oriented dimers. This point is also supported by the fact that the ring disappeared when the duration of the sample gas pulse was set too short to maintain efficient adiabatic cooling for the creation of dimers. The ring gradually appeared as the gas pulse duration was increased. Thus, the observed ring is attributed to Ar^+ from Coulomb exploded Ar_2. Contribution of the trimer or larger clusters could not be completely excluded from the gas-load dependence. However, as mentioned later, no noticeable signals from larger clusters were observed in rotational spectra. With regard to fragmentation pathways in Coulomb explosion, there is no other ring inside. So we securely assign the observed ring as Ar^+ from the dissociation channel of $Ar_2^{2+} \rightarrow Ar^+ + Ar^+$, with the smallest kinetic energy release (KER) in Coulomb explosion. The KER value for the observed ring is estimated to be < 5 eV, which essentially agrees with the previous studies.[42] The angular distribution was evaluated only with the ions detected between the two dashed rings in Fig. 2a.

The radial distribution of ion images contains information on KER distribution, which is useful to identify Coulomb explosion channels and to characterize a probability distribution pertinent to a vibrational wave function.[42, 43] In the present study, however, our high count-rate condition led to ineligible space charge effect (mostly by Ar^+ ions from monomers) on ring radius of Ar^+ from dimers. Although the most probable kinetic energy of Ar^+ in the ring is estimated, the laser power and sample-gas density affected the extent of the space charge effect, and it was not possible to completely eliminate the effect to evaluate reliable KER distribution. We note even with the space-charge perturbation, observed angular distributions well reflect rotational dynamics as mentioned below.

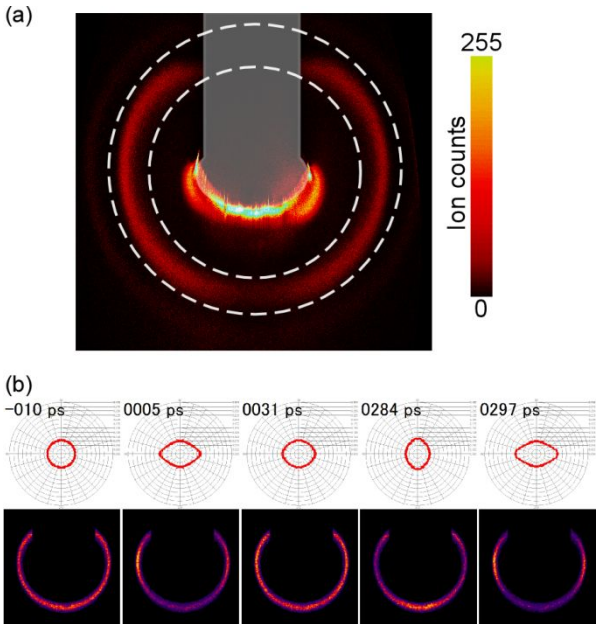

Fig. 2 (a) Probe-only ion image of Ar^+. Shaded area displays the masked region. Two concentric, dashed circles limit the region of interest, and only ions detected between two circles are used to evaluate the angular distribution. (b) Selected snapshots of rotational wave-packet dynamics of Ar_2 created with a linearly polarized pump pulse. (Lower) Ar^+ ion images. (Upper) Polar plots of angular distributions derived from the Ar^+ ion images. The up/down symmetrisation is adopted to complement the masked region. Pump pulse was linearly polarized along the horizontal direction in the images, while probe was circularly polarized in the imaged plane.

Figure 2b shows selected ion images and corresponding angular distributions in the polar coordinate representation. Before the pump-pulse irradiation, ion distribution is isotropic, reflecting random orientation of the interatomic axis of Ar_2 in the molecular beam. Upon the linearly polarized (along the horizontal direction in Fig. 2b) pump irradiation, rotational wave packet dynamics was initiated. The observed dynamics shows characteristic behaviors as have been reported for rotational wave packets in diatomic systems excited with a linearly polarized pulse.[29-33] Just after the pump irradiation, the dimer axis starts to align along the polarization direction, and then the aligned (localized) packet is rapidly dispersed. After that, alignment, anti-alignment, and dispersion dynamics are repeated periodically.

Time evolution of rotational wave-packet dynamics is also well characterized with time-dependent alignment parameters, $\langle\cos^2\theta\rangle$ and $\langle P_n(\cos\theta)\rangle$, where P_n is a Legendre polynomial with an even n, θ is defined as an angle from the polarization vector of the pump pulse, and $\langle\ldots\rangle$ indicates ensemble averaging.[30, 44] It is noted that $\cos^2\theta = [2P_2(\cos\theta) + 1]/3$. Figure 3a (left) shows time-dependent $\langle\cos^2\theta\rangle$ up to 1 ns, evaluated from the observed time-resolved images. Randomly oriented ensembles give $\langle\cos^2\theta\rangle = 1/3$. Aligned and anti-aligned ensembles lead to larger and smaller values of $\langle\cos^2\theta\rangle$, respectively. In the time trace, revivals with the period of ~290 ps can be clearly seen as in the previous studies.[29, 30] Figures 3b,c (left) show time traces for $\langle P_4(\cos\theta)\rangle$ and $\langle P_6(\cos\theta)\rangle$, respectively. An ensemble average of the n-th order polynomials highlights the coherence between two rotational eigenstates whose rotational quantum numbers

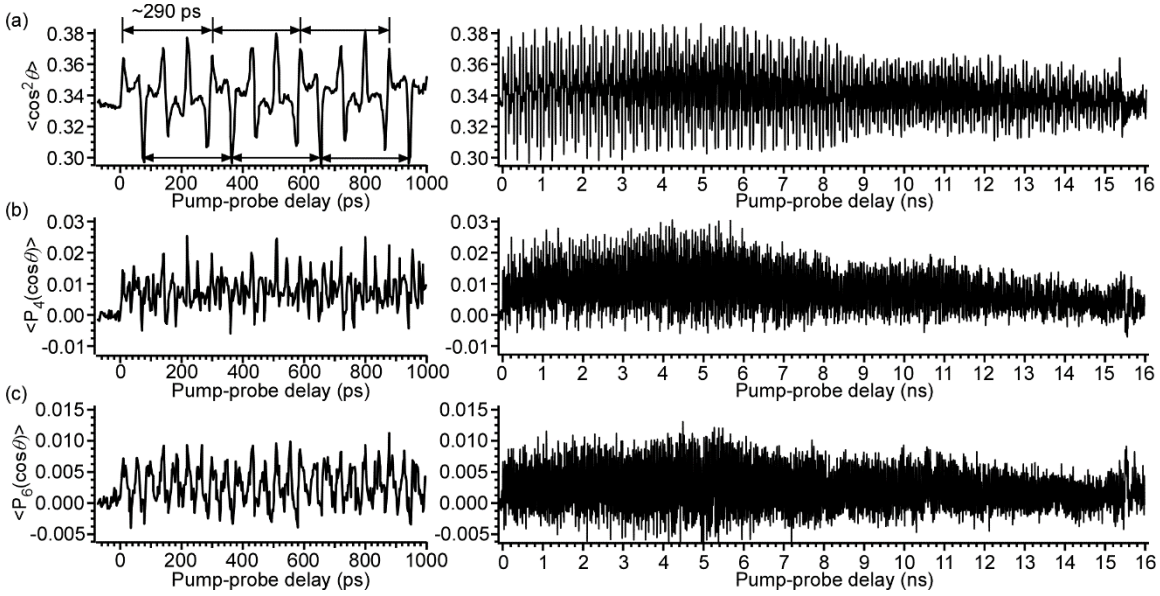

Fig. 3 Time-dependent alignment parameters: (a) $\langle\cos^2\theta\rangle$, (b) $\langle P_4(\cos\theta)\rangle$, and (c) $\langle P_6(\cos\theta)\rangle$.

J'' and J' satisfy that $\Delta J = J' - J''$ is even and $\leq n$. The time traces for $\langle P_4(\cos\theta)\rangle$ and $\langle P_6(\cos\theta)\rangle$, therefore, contain higher frequency components due to interferences between states with larger ΔJ (= 4 and 6). The base lines of the alignment parameters are raised for positive delay from those for isotropic orientation in negative delay, i.e., $\langle\cos^2\theta\rangle = 1/3$ and $\langle P_4(\cos\theta)\rangle = \langle P_6(\cos\theta)\rangle = 0$. This finding is a manifestation of permanent alignment via the nonadiabatic excitation by a linearly polarized pulse.[33]

Figures 3a–c (right) show the time traces of the same alignment parameters for the whole delay range of up to 16 ns, corresponding to more than 50 revival periods. Oscillation lasts for longer than 15 ns. Frequency resolution higher than 100 MHz is, therefore, expected for Fourier transformed spectra. We note that the oscillation amplitudes of the time traces show fluctuation and become smaller in longer delay. Such degradation of the oscillations comes from several possible origins. Effects of the centrifugal distortion, which perturbs rigid rotor energy levels, lead to dephasing of revival dynamics.[45, 46] Loss of the pump-probe overlap and a beam drift during the scan also degrades the oscillation. In particular, the observed oscillation suddenly diminishes at around 15.5 ns. Such an abrupt change may be attributed to the imperfect flatness of the mechanical stages. There have been several ways to improve the contrast of the time traces: for example, the use of an elaborated molecular-beam tracking system will be effective.[47, 48] Still, the present trace have enough time window to achieve one-order higher frequency resolution than the previous studies after Fourier transformation (FT).

Figure 4 shows frequency-domain rotational spectra of Ar_2, obtained as FT of the time traces of $\langle\cos^2\theta\rangle$, $\langle P_4(\cos\theta)\rangle$, and $\langle P_6(\cos\theta)\rangle$. As shown in the inset in Fig. 4a, effective frequency resolution is ~90 MHz, as intended in the present setup. Owing to the broad bandwidth of the ultrashort pump pulse, frequency range of 0–200 GHz was covered in a single measurement. Spectral assignments for Fig. 4 are simply done with the energy level expression of diatomic molecules: $E_J = B_0 J(J+1) - D_0 J^2(J+1)^2$. The noticeable peaks for $\langle\cos^2\theta\rangle$, $\langle P_4(\cos\theta)\rangle$, and $\langle P_4(\cos\theta)\rangle$ are assigned to the beat frequencies between J'' and J' states, where ΔJ = 2, 2 and 4, and 2, 4, 6, respectively, as labelled in Fig. 4. Due to the nuclear spin statistics, only even J states are allowed for $^{40}Ar_2$.[23,25] The small signals with $\Delta J = 4$ (*e.g.* $10 - 6$ and $10 - 4$) for $\langle\cos^2\theta\rangle$ may be due to small deviation in the observed images from genuine angular distribution.

The peak positions in Fig. 4 are determined with 0.1 MHz precision by Gaussian fitting to the top part of each peak. Absolute peak frequencies vary by up to ~10 MHz from day to day, due to the instability in optical delay lines as mentioned in the Experimental section. To check the reproducibility and compensate the day-to-day fluctuation, four independent measurements were carried out. Spectroscopic constants B_0 and D_0 were determined via a least-squares regression using all the observed peaks of each measurement. Differences between the observed and calculated frequencies are all within 10 MHz, validating the fitting results. The four sets of B_0 and D_0 are the same within the standard deviations of the fits. Then, they are averaged to give the final results: B_0 = 1.72713(9) GHz and D_0 = 0.310(5) MHz. Here uncertainties, given in parentheses for the last digits, have been evaluated from the standard deviations of each fits and that of the average of the four sets. The B_0 and D_0 constants in cm^{-1} unit are also listed in Table 1. Observed peak frequencies, derived as an average for the four measurements, and those calculated by using the determined constants are summarized in Table 2.

The B_0 constant determined in the present study is consistent with the results from the previous rotational wave-packet imaging studies,[29, 30] while the precision has been much improved (more than 10 times), as shown in Table 1. The value from the VUV-LIF measurements is outside the margin of the experimental uncertainty quoted therein.[25] Such a discrepancy would be attributed to the exclusion of low-J transitions and

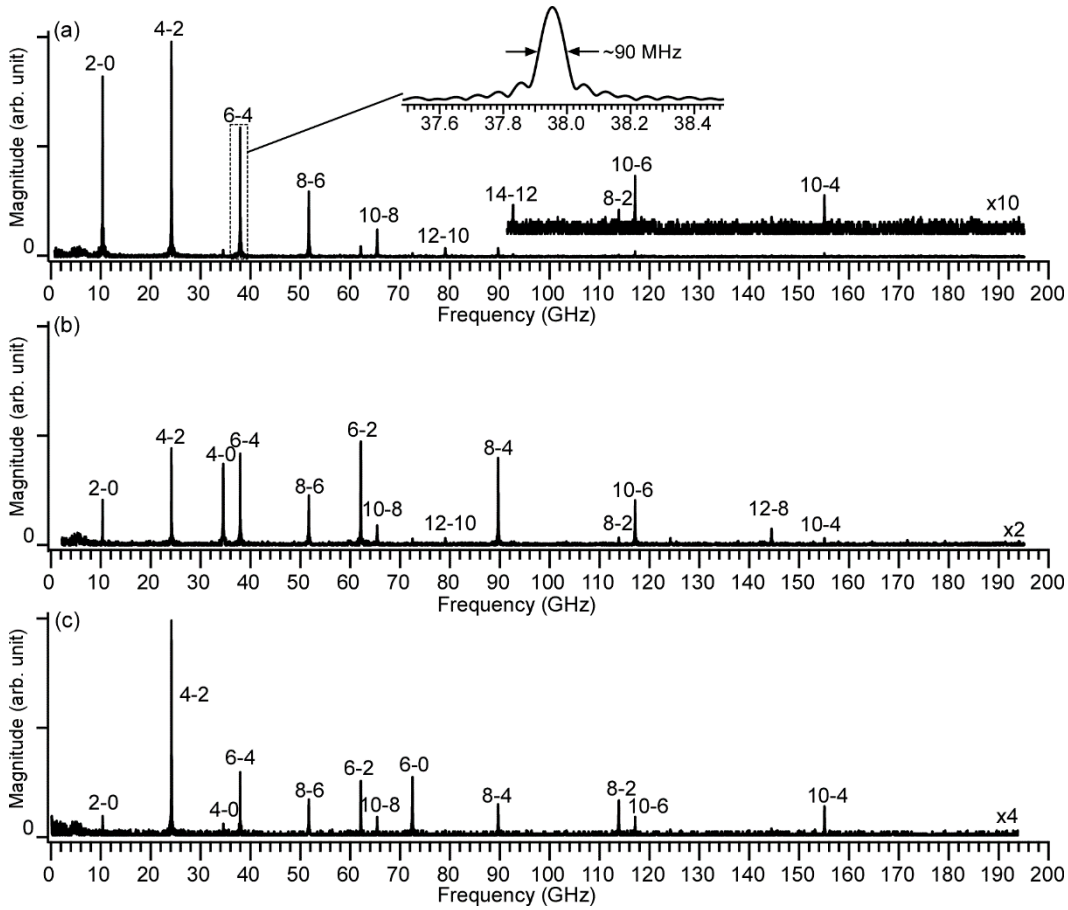

Fig. 4 Power spectra derived by Fourier transformation of the time-dependent alignment parameters in Fig.3, corresponding rotational spectra of Ar_2: (a-c) spectra from $\langle\cos^2\theta\rangle$, $\langle P_4(\cos\theta)\rangle$, and $\langle P_6(\cos\theta)\rangle$, respectively. Peak frequencies correspond to the energy differences of two states involved in a wave packet. For each peak, connected two states are shown as J'–J'', where J' and J'' indicate their rotational (angular momentum) quantum numbers. Inset in (a) represents a zoom up around the J = 6–4 peak. The full-width at half-maximum (FWHM) of the line is ~90 MHz, indicating the effective frequency resolution of the present measurements.

neglect of the higher-order effect in centrifugal distortion, as mentioned in the reanalysis.[10] In contrast, the reanalysis of the VUV-LIF data provided the B_0 and D_0 constants, [10] both of which agree well with the present results, as seen in Table 1. This mutual consistency between two different experimental approaches validates the accuracy of the results.

Table 2. Observed and calculated frequencies for J'–J'' peaks with determined spectroscopic constants of Ar_2 (in GHz).[a]

J'	J''	Obs	Calc	Obs−Calc
2	0	10.3619	10.3620	0.0001
4	2	24.1696	24.1692	0.0004
6	4	37.9534	37.9554	-0.0020
8	6	51.7090	51.7085	0.0005
10	8	65.4158	65.4167	-0.0009
12	10	79.0682	79.0679	0.0003
14	12	92.6517	92.6501	0.0016
4	0	34.5410	34.5311	0.0098
6	2	62.1265	62.1245	0.0020
8	4	89.6572	89.6639	-0.0067
10	6	117.1246	117.1253	-0.0007
12	8	144.4843	144.4846	-0.0004
14	10	171.7181	171.7180	0.0001
6	0	72.4837	72.4865	-0.0027
8	2	113.8375	113.8331	0.0045
10	4	155.0799	155.0806	-0.0007
		B_0	1.72713(9)	
		D_0	$3.10(5) \times 10^{-4}$	

[a] Obs: observed frequency, as an average of four independent measurements, and Calc: calculated frequency based on the spectroscopic constants determined in the present study, as listed.

The improvement of B_0 and D_0 values is of fundamental importance since it offers stringent references for evaluating theories and serve as indispensable sources for the construction of accurate empirical potential. The recent extensive *ab initio* calculations (CCSDT(Q) or higher levels) predicted the B_0 values, which agree remarkably well with the present result.[16] This validates the accuracy of the potentials derived therein, in particular, regarding the location of their minimum (with the equilibrium interatomic distance of 376.2 pm). Quite recently, bound states of Ar_2 were calculated on reported potentials by solving the Lippmann-Swinger integral equation in momentum space.[26] The predicted energy levels based on the potential by Patkowski et al.[18] are fit with the B_0 and D_0 constants, as listed in Table 1, in astonishing agreement with the present results. This manifests the status of state-of-the-art theoretical studies on interatomic interactions and relevant rovibrational energy-level calculations. It is noted that the calculated rotational constants based on the CCSD(T) levels show some deviations

from the experimental value, while the CCSD(T) level is sometimes regarded as a standard. It has been already reported that a post-CCSD(T) level is required to precisely predict high-resolution spectra of weakly-bound molecular clusters.[49] The present results could be used to evaluate post-CCSD(T) calculation-based potentials.

The present wave-packet imaging of Ar_2 deserves possible advances in several directions. First, creation and observation of wave packets including higher-*J* states may lead to more precise determination of spectroscopic constants, in particular, higher-order terms in centrifugal distortion, which sensitively depend on anharmonic nature of the interatomic potential. More extensive rotational excitation can be realized simply by raising pump-pulse intensity, or by using a pulse train or designed pulses. [35, 50-52] Second, in principle, the present approach will be also applicable for observation of vibrational wave-packet dynamics, once the pump pulse duration is reduced enough to induce nonadiabatic excitation for vibrational motion, of which period is estimated to be ~1 ps from the reported vibrational energy intervals.[25] Efficiency of vibrational Raman excitation is generally weaker than the rotational Raman, and then, effective control method and/or highly sensitive observation method would be required. For observation of the vibrational wave-packet, mapping out the KER of fragmented Ar^+ in time-resolved manner will be much beneficial. Actually, vibrationally averaged interatomic distance of Ar_2 was evaluated through the KER measurements by COLTRIMS.[42] The KER measurements was also implemented quite recently to characterize vibrational wave functions for H_2 and rare-gas dimers.[43]

4 Conclusions

We report time-domain rotational spectroscopy of the argon dimer, by adopting Coulomb explosion imaging of rotational wave-packet dynamics. Using the high-throughput slice imaging apparatus and the folded optical delay line, wave-packet movies were taken for the pump-probe delay up to ~16 ns. Periodic oscillation of the alignment parameters last for more than 15 ns. Power spectra from Fourier transformation of the time traces of the alignment parameters gives rotational spectra of Ar_2 with spectral resolution down to ~90 MHz. From the spectra, the rotational constant and the centrifugal distortion constant are determined to be 1.72713(9) GHz [0.057611(4) cm^{-1}] and 0.0310(5) MHz [1.03(2) × 10^{-6} cm^{-1}], respectively, being much improved in precision than the previous experiments. The determined values are a finest test ground of state-of-the-art theoretical calculation, and will be important sources for the construction of an accurate empirical intermolecular potential. We note that the present approach has opened a new way to observed rotational spectra of molecular systems, even if without permanent dipoles nor chromophores suitable for applying vibrational or electronic spectroscopies. High resolution spectroscopy based on the combination of impulsive Raman and Coulomb explosion imaging has been recently reported for rare gas dimers,[29, 30] $(CS_2)_2$,[53] C_2H_2-He,[54] and $(CS_2)_2$ in a helium droplet,[55] showing versatility of the approach. This study also demonstrates superior frequency resolution of the present method than frequency-domain Raman spectroscopy and vibronic spectroscopy with pulsed lasers. These points provide potential advantage for further implication of the present method.

Author Contributions

Kenta Mizuse: Conceptualization; Data curation; Formal analysis; Funding acquisition; Investigation; Methodology; Project administration; Resources; Software; Supervision; Validation; Visualization; Writing - original draft. Urara Sato: Formal analysis; Investigation. Yuya Tobata: Investigation. Yasuhiro Ohshima: Conceptualization; Formal analysis; Funding acquisition; Investigation; Methodology; Project administration; Resources; Software; Supervision; Validation; Writing - review & editing.

Conflicts of interest

There are no conflicts to declare.

Acknowledgements

We thank members of the Equipment Development Center in Institute for Molecular Science for their contribution to the construction of the apparatus. This work was financially supported by JSPS/MEXT KAKENHI (Grant Nos. JP21K18938, JP21H05434, JP20K21169, JP19K22164 and JP18H03897) and the Core-to-Core program (JPJSCCA20210004), JST SPRING (Grant No. JPMJSP2106), the Shimadzu Science Foundation, the Harmonic Ito Foundation, the Fujikura Foundation, Kitasato University Research Grant for Young Researchers, and the Yoshinori Ohsumi Fund for Fundamental Research in TokyoTech.

References

1. G. C. Maitland, M. Rigby, E. B. Smith and W. A. Wakeham, *Intermolecular Forces*, Clarendon Press, Oxford, 1981.
2. A. Stone, *The Theory of Intermolecular Forces, 2nd Ed.*, Oxford University Press, Oxford, 2013.
3. R. A. Aziz, in *Inert Gases: Potentials, Dynamics, and Energy Transfer in Doped Crystals*, Springer, Berlin, 1984, ch. 2.
4. J. Barker and A. Pompe, *Aust. J. Chem.*, 1968, **21**, 1683–1694.
5. G. C. Maitland and E. B. Smith, *Mol. Phys.*, 1971, **22**, 861–868.
6. J. M. Parson, P. E. Siska and Y. T. Lee, *J. Chem. Phys.*, 1972, **56**, 1511–1516.
7. R. A. Aziz and H. H. Chen, *J. Chem. Phys.*, 1977, **67**, 5719–5726.
8. K. T. Tang and J. P. Toennies, *J. Chem. Phys.*, 1984, **80**, 3726–3741.
9. R. A. Aziz, *J. Chem. Phys.*, 1993, **99**, 4518–4525.
10. S. J. Boyes, *Chem. Phys. Lett.*, 1994, **221**, 467–472.
11. K. T. Tang and J. P. Toennies, *J. Chem. Phys.*, 2003, **118**, 4976–4983.

12. P. T. Myatt, A. K. Dham, P. Chandrasekhar, F. R. W. McCourt and R. J. Le Roy, *Mol. Phys.*, 2018, **116**, 1598–1623.
13. S. M. Cybulski and R. R. Toczyłowski, *J. Chem. Phys.*, 1999, **111**, 10520–10528.
14. P. Slavíček, R. Kalus, P. Paška, I. Odvárková, P. Hobza and A. Malijevský, *J. Chem. Phys.*, 2003, **119**, 2102–2119.
15. K. Patkowski, G. Murdachaew, C.-M. Fou and K. Szalewicz, *Mol. Phys.*, 2005, **103**, 2031–2045.
16. B. Jäger, R. Hellmann, E. Bich and E. Vogel, *Mol. Phys.*, 2009, **107**, 2181–2188.
17. E. Vogel, B. Jäger, R. Hellmann and E. Bich, *Mol. Phys.*, 2010, **108**, 3335–3352.
18. K. Patkowski and K. Szalewicz, *J. Chem. Phys.*, 2010, **133**, 094304.
19. W. Jäger, Y. Xu and M. C. L. Gerry, *J. Chem. Phys.*, 1993, **99**, 919–927.
20. J. U. Grabow, A. S. Pine, G. T. Fraser, F. J. Lovas, R. D. Suenram, T. Emilsson, E. Arunan and H. S. Gutowsky, *J. Chem. Phys.*, 1995, **102**, 1181–1187.
21. Y. Xu, W. Jäger, J. Djauhari and M. C. L. Gerry, *J. Chem. Phys.*, 1995, **103**, 2827–2833.
22. Y. Tanaka and K. Yoshino, *J. Chem. Phys.*, 1970, **53**, 2012–2030.
23. E. A. Colbourn and A. E. Douglas, *J. Chem. Phys.*, 1976, **65**, 1741–1745.
24. D. E. Freeman, K. Yoshino and Y. Tanaka, *J. Chem. Phys.*, 1979, **71**, 1780–1793.
25. P. R. Herman, P. E. LaRocque and B. P. Stoicheff, *J. Chem. Phys.*, 1988, **89**, 4535–4549.
26. T. Sahraeian and M. R. Hadizadeh, *Int. J. Quantum Chem*, 2019, **119**, e25807.
27. H. P. Godfried and I. F. Silvera, *Phys. Rev. Lett.*, 1982, **48**, 1337‑1340.
28. H. P. Godfried and I. F. Silvera, *Phys. Rev. A*, 1983, **27**, 3008.
29. J. Wu, A. Vredenborg, B. Ulrich, L. P. H. Schmidt, M. Meckel, S. Voss, H. Sann, H. Kim, T. Jahnke and R. Dörner, *Phys. Rev. A*, 2011, **83**, 061403.
30. A. v. Veltheim, B. Borchers, G. Steinmeyer and H. Rottke, *Phys. Rev. A*, 2014, **89**, 023432.
31. F. Rosca-Pruna and M. Vrakking, *Phys. Rev. Lett.*, 2001, **87**, 153902.
32. F. Rosca-Pruna and M. J. J. Vrakking, *J. Chem. Phys.*, 2002, **116**, 6567–6578.
33. P. W. Dooley, I. V. Litvinyuk, K. F. Lee, D. M. Rayner, M. Spanner, D. M. Villeneuve and P. B. Corkum, *Phys. Rev. A*, 2003, **68**, 023406.
34. H. Stapelfeldt and T. Seideman, *Rev. Mod. Phys.*, 2003, **75**, 543–557.
35. Y. Ohshima and H. Hasegawa, *Int. Rev. Phys. Chem.*, 2010, **29**, 619–663.
36. C. P. Koch, M. Lemeshko and D. Sugny, *Rev. Mod. Phys.*, 2019, **91**, 035005.
37. K. Mizuse, R. Fujimoto and Y. Ohshima, *Rev. Sci. Instrum.*, 2019, **90**, 103107.
38. K. Mizuse, R. Fujimoto, N. Mizutani and Y. Ohshima, *J. Vis. Exp.*, 2017, **120**, e54917.
39. K. Mizuse, K. Kitano, H. Hasegawa and Y. Ohshima, *Sci. Adv.*, 2015, **1**, e1400185
40. P. E. Ciddor, *Appl. Opt.*, 1996, **35**, 1566–1573.
41. U. Even, J. Jortner, D. Noy, N. Lavie and C. Cossart-Magos, *J. Chem. Phys.*, 2000, **112**, 8068–8071.
42. B. Ulrich, A. Vredenborg, A. Malakzadeh, L. P. H. Schmidt, T. Havermeier, M. Meckel, K. Cole, M. Smolarski, Z. Chang, T. Jahnke and R. Dörner, *J. Phys. Chem. A*, 2011, **115**, 6936–6941.
43. S. Zeller, M. Kunitski, J. Voigtsberger, M. Waitz, F. Trinter, S. Eckart, A. Kalinin, A. Czasch, L. P. H. Schmidt, T. Weber, M. Schöffler, T. Jahnke and R. Dörner, *Phys Rev Lett*, 2018, **121**, 083002.
44. A. S. Mouritzen and K. Mølmer, *J. Chem. Phys.*, 2006, **124**, 244311.
45. W. Jarzęba, V. V. Matylitsky, A. Weichert and C. Riehn, *Phys. Chem. Chem. Phys.*, 2002, **4**, 451-454.
46. D. S. Kummli, H. M. Frey and S. Leutwyler, *J. Chem. Phys.*, 2006, **124**, 144307.
47. C. Schröter, J. C. Lee and T. Schultz, *Proc. Natl. Acad. Sci. USA*, 2018, **115**, 5072–5076.
48. J. C. Lee, D. E. Lee and T. Schultz, *Phys. Chem. Chem. Phys.*, 2019, **21**, 2857-2860.
49. P. Jankowski, A. R. W. McKellar and K. Szalewicz, *Science*, 2012, **336**, 1147-1150.
50. J. P. Cryan, P. H. Bucksbaum and R. N. Coffee, *Phys. Rev. A*, 2009, **80**, 063412.
51. C. Bloomquist, S. Zhdanovich, A. A. Milner and V. Milner, *Phys. Rev. A*, 2012, **86**, 063413.
52. A. A. Milner, A. Korobenko and V. Milner, *Phys. Rev. A*, 2016, **93**, 053408.
53. A. S. Chatterley, M. O. Baatrup, C. A. Schouder and H. Stapelfeldt, *Phys. Chem. Chem. Phys.*, 2020, **22**, 3245-3253.
54. G. Galinis, C. Cacho, R. T. Chapman, A. M. Ellis, M. Lewerenz, L. G. Mendoza Luna, R. S. Minns, M. Mladenović, A. Rouzée, E. Springate, I. C. E. Turcu, M. J. Watkins and K. von Haeften, *Phys. Rev. Lett.*, 2014, **113**, 043004.
55. A. S. Chatterley, L. Christiansen, C. A. Schouder, A. V. Jørgensen, B. Shepperson, I. N. Cherepanov, G. Bighin, R. E. Zillich, M. Lemeshko and H. Stapelfeldt, *Phys. Rev. Lett.*, 2020, **125**, 013001.